Journal of
Marine Science and Engineering

MDPI

Article

Stability Analysis in a Direct-Current Shipboard Power System with Parallel Permanent Magnet Synchronous Generators and Supercapacitor Integration

Qinsheng Yun [1,2,*], Xiangjun Wang [1,*], Shenghan Wang [2], Wei Zhuang [2] and Wanlu Zhu [3]

[1] School of Electrical Engineering, Naval University of Engineering, Wuhan 430030, China
[2] Shanghai Marine Diesel Engine Research Institute, Shanghai 201108, China; 15551525111@163.com (S.W.); headings@163.com (W.Z.)
[3] College of Automation, Jiangsu University of Science and Technology, Zhenjiang 212100, China; zhuwanlu@just.edu.cn
* Correspondence: yunqinsheng@126.com (Q.Y.); wxjnue@163.com (X.W.)

Abstract: This paper investigates the small-signal stability of a DC shipboard power system (SPS) with the integration of a supercapacitor. As an efficient energy storage solution, supercapacitors can not only provide rapid energy response to sudden power demand spikes, effectively mitigating load fluctuations, but also enhance the system's resilience to disturbances. In the context of the parallel operation of two Permanent Magnet Synchronous Generators (PMSGs), the inclusion of supercapacitors may alter the system's dynamic behaviors, thereby affecting its small-signal stability. This paper develops the small-signal model of SPS and explores the small-signal model under various power distribution strategies in the parallel operation of diesel generator sets. Through the calculation of eigenvalues and influence factors, the system's oscillation modes are analyzed, and key parameters affecting the stability of the DC distribution system are identified. Furthermore, this paper meticulously examines the specific impacts of electrical and control parameter variations on the system's small-signal stability. Simulation experiments validate the accuracy of the small-signal stability analysis after supercapacitor integration into SPS.

Keywords: DC distribution shipboard power systems; supercapacitors; generators parallel operation; small-signal stability

check for updates

Citation: Yun, Q.; Wang, X.; Wang, S.; Zhuang, W.; Zhu, W. Stability Analysis in a Direct-Current Shipboard Power System with Parallel Permanent Magnet Synchronous Generators and Supercapacitor Integration. *J. Mar. Sci. Eng.* **2024**, *12*, 578. https://doi.org/10.3390/jmse12040578

Academic Editor: Rosemary Norman

Received: 29 February 2024
Revised: 26 March 2024
Accepted: 27 March 2024
Published: 29 March 2024

1. Introduction

With the increasing demand for electrical power in ships and the growing stringency of environmental regulations, new solutions are needed for the future development of shipboard power systems (SPSs) [1–4]. The DC distribution SPS, as an independent power system with limited inertia, exhibits good angular stability [5], enhancing the efficiency and reliability of SPSs [6–8], and is poised to become a developmental trend in future marine power systems [9]. However, propulsion loads, acting as constant power loads (CPLs), exhibit negative incremental impedance, destabilizing the DC bus voltage. This issue is exacerbated by variations in CPLs due to changes in motor speed or torque, particularly in maritime environments [10].

During the operation of DC SPSs, the system frequently encounters minor disturbances resulting from random load changes, adjustment reactions of generator sets, and variations in transmission line spacing due to natural causes [11–14]. Although these disturbances do not fundamentally alter the overall structure of the electrical system, they can lead to varying degrees of oscillations in electrical quantities. The unique operating environment of maritime vessels complicates SPS operation, demanding higher reliability and stability. Failure to swiftly restore stability after minor disturbances during stable operation may result in system failure, jeopardizing the safety of onboard personnel and hindering vessel navigation. Analyzing and calculating the stability status of the system under various conditions is critical to ensuring its stable operation, given the characteristics of DC power distribution systems. Therefore, conducting small-signal stability analyses of DC distribution SPSs is paramount to guarantee stable operation under diverse operational conditions.

Currently, two main methods are utilized for the small-signal stability analysis of an SPS: eigenvalue analysis based on the time domain and impedance analysis grounded in the frequency domain [15,16]. The utilization of eigenvalue analysis offers distinct advantages, notably its ability to provide comprehensive insight into the system's stability by directly assessing the behavior of eigenvalues. This method allows for a precise determination of the system's response to small perturbations, facilitating the identification of stability margins and critical system parameters that influence stability.

Recent studies on the stability analysis of the DC SPS investigated the effects of design parameters on system stability [17,18]. An eigenvalue analysis for a hybrid power SPS incorporating virtual synchronous machines was performed to examine the impact of the voltage controller, line reactance, and virtual reactance on system stability [19]. The stability of a hybrid DC SPS equipped with energy storage systems was assessed through a hybrid H-matrix model, focusing on the influence of energy storage working mode and inverter current controller parameters on system stability [20].

Small-signal stability analyses are also executed for SPSs operating with generator sets in parallel. To address stability issues arising from the parallel operation of inverters with synchronous generators, small-signal models have been developed for variable-speed generator set parallel systems, analyzing stability across different system configurations [21]. Small-signal models for synchronous generators are established by paralleling two isolated inverters, enabling calculation of participation factors and conducting an eigenvalue sensitivity analysis and small-signal stability analysis [22]. A parameter design strategy for parameterizing parallel virtual synchronous generator systems was articulated in [23], factoring in both AC and DC constraints, thereby delineating detailed stability boundaries through small-signal modeling. These studies primarily focused on synchronous generators and their operation in parallel, neglecting the effects of power distribution among Permanent Magnet Synchronous Generators (PMSGs) on stability, particularly when PMSGs are connected to fully controlled rectifiers involving multiple control loops.

Supercapacitors, as high-performance energy storage devices, contribute to the rapid development of low-power electronic products (wearables, portable electronic devices) and high-power military applications (guided missile technology and techniques) [24]. Serving as buffer elements, they help stabilize the voltage of the DC bus and reduce fluctuations between power sources and loads, thus enhancing the overall stability and reliability of the system. The addition of supercapacitors in DC distribution systems may induce changes in the system's dynamic characteristics, impacting small-signal stability. A small-signal model for a battery and supercapacitor hybrid energy storage system employing a master-slave control scheme was proposed, analyzing the effects of controller and filter parameter variations on system performance using frequency-domain analysis [25]. This methodology was extended to the small-signal modeling and control of battery-supercapacitor systems within DC microgrids [26]. A distributed cooperative control framework for multiple dc electric springs in a dc microgrid was established and analyzed for small-signal stability in [27], with system stability effects of communication weight demonstrated through an eigenvalue analysis.

While existing studies on the integration of a supercapacitor into a DC SPS have laid a foundational understanding of its impact on small-signal stability, research primarily targets individual hybrid energy storage systems, leaving the broader implications of SPS stability less explored. The integration of a supercapacitor into an SPS and its consequent effect on the stability has been insufficiently considered. Existing analyses often overlook the nuanced impacts of newly introduced electrical and control parameters, such as the input-output characteristics of converters and the parameters of PI controllers for supercapacitors on system stability. These parameters play a crucial role in the operational efficiency and stability of SPSs, especially when integrated with supercapacitors.

This paper proposes a small-signal stability analysis method based on the integration of supercapacitors into a marine DC SPS under parallel operation of PMSGs, investigating the specific impact of newly introduced electrical and control parameters by a supercapacitor on system stability. The main contributions can be summarized as follows:

(1) This paper develops detailed control and small-signal models for PMSGs operating in parallel across five distinct power allocation modes, offering a nuanced understanding of system behavior under various operational scenarios.
(2) This paper rigorously analyzes how newly introduced electrical and control parameters, such as converters' input-output characteristics and supercapacitor PI controller settings, impact system stability after supercapacitor integration, identifying key factors influencing system resilience and stability.
(3) The system stability analysis results are validated by MATLAB simulations and comparative analyses, confirming the supercapacitor-introduced parameters' impact on stability and showing how precise control parameter adjustments can enhance stability and identify critical thresholds.

The structure of this paper is organized as follows. Section 2 elaborates on the topology of DC SPS and the small-signal model of the parallel operation of PMSGs, discussing five main power allocation methods. Section 3 establishes the small-signal model for integrating SC into a DC SPS with parallel-operating PMSGs and analyzes the implications of this integration on the system's small-signal stability. Section 4 explores the impact of parameter variations on system stability, presenting both a simulation analysis and experimental findings. Section 5 concludes this paper.

2. System Configuration and Mathematical Model

The structural diagram of the DC SPS is illustrated in Figure 1. The system consists of two PMSGs, each connected to the DC bus through a fully controlled rectifier (AC/DC converter). Supercapacitors are connected to the DC bus via a bidirectional DC/DC converter. The DC bus serves as the central hub of the system, linking all power sources and loads, including the Variable Frequency Drives (VFDs) used for propulsion motors.

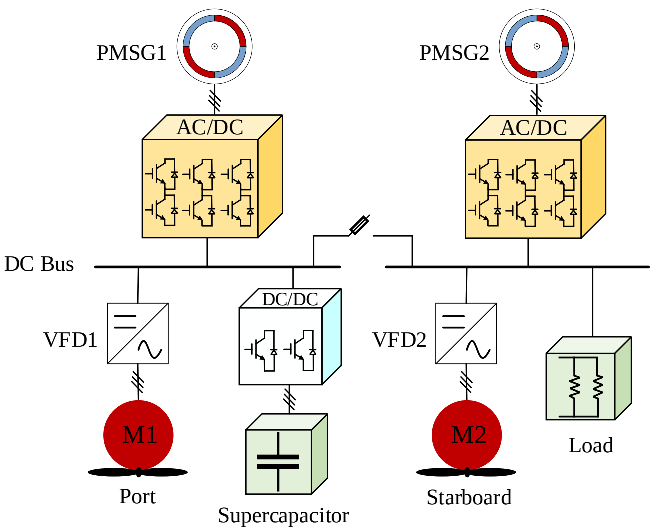

Figure 1. Structure diagram of DC distribution of SPS.

The methodology for the small-signal stability analysis of this DC SPS under investigation is delineated in the flowchart presented in Figure 2.

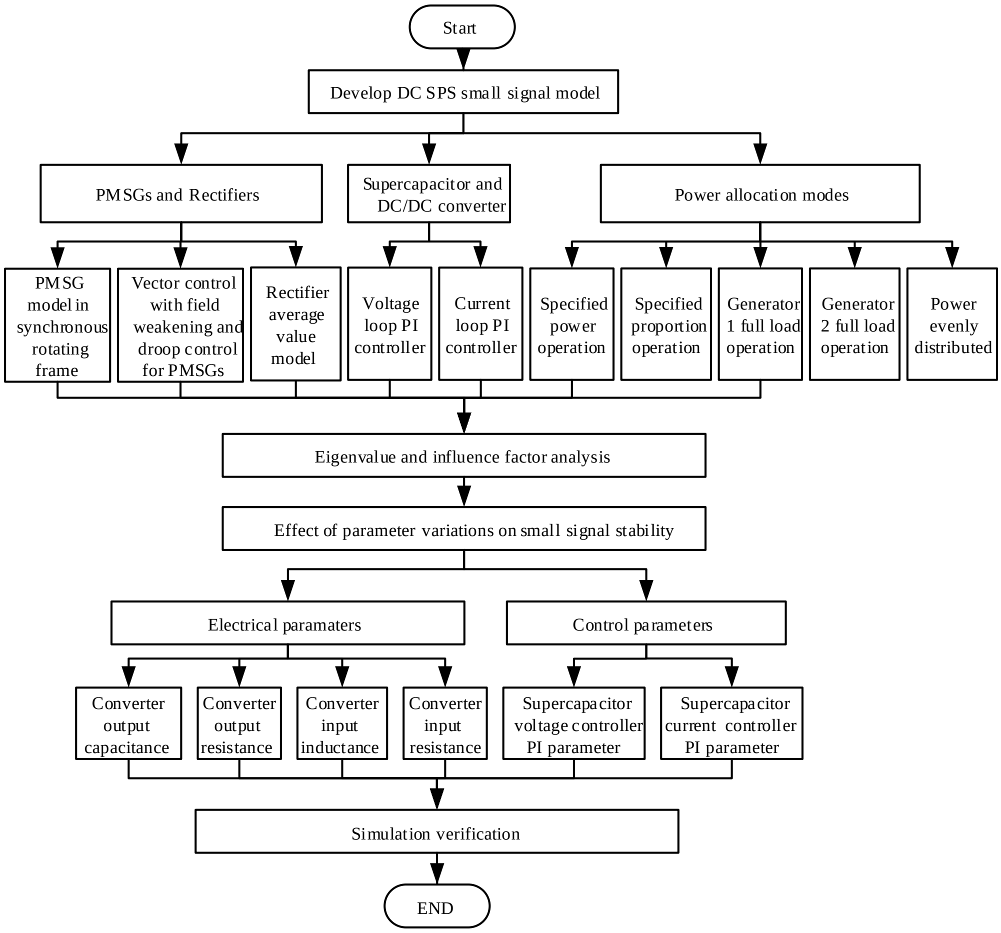

Figure 2. Flowchart of small-signal stability analysis for DC SPS.

2.1. PMSG and Rectifier Model

In this paper, the modeling of the PMSG is conducted in the synchronous rotating coordinate system [28]. The stator voltage equation of the PMSG is expressed as follows:

$$\begin{cases} u_d = Ri_d + L_d \frac{d}{dt} i_d - \omega_e L_q i_q \\ u_q = Ri_q + L_q \frac{d}{dt} i_q + \omega_e (L_d i_d + \psi_f) \end{cases} \tag{1}$$

where i_d, i_q and u_d, u_q are the stator currents and voltages in the d and q axes; ψ_f is the permanent magnets flux; R is the stator resistance; L_d and L_q are the stator leakage inductances in the d and q axes; and ω_e is the rotor electrical angular speed.

In this study, the control model for PMSGs incorporates both flux-weakening and droop control mechanisms based on vector control principles [10]. As shown in Figure 3, the control of the rectifier is implemented using four PI controllers; this structure comprises two inner-loop current controllers for the decoupling of dq-axis current control. The outer loop includes a flux-weakening controller, which limits the machine voltage during high-speed operation, and a droop controller that adjusts the DC voltage reference value to achieve power distribution during parallel operation of PMSGs. The implementation of the flux-weakening control mitigates the risk of excessive terminal or DC bus voltages under high-speed conditions, expanding the operational voltage range and ensuring safe operation within the system limits. The droop control, crucial for parallel-operating PMSGs in the DC SPS, automatically adjusts power output in response to load variations, enabling balanced power distribution and maintaining system stability without the need for direct communication between units.

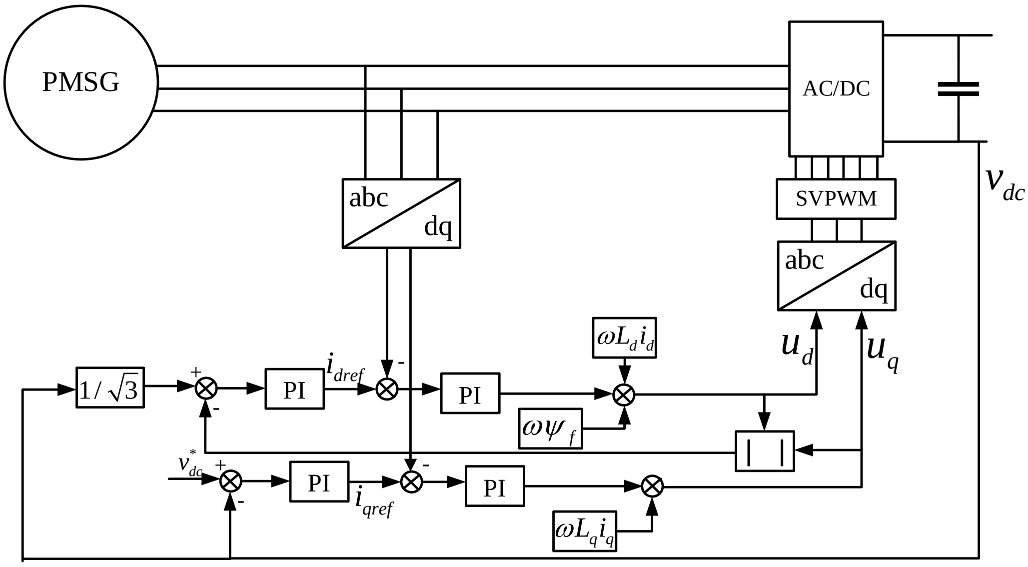

Figure 3. Control diagram of PMSG.

The differential equation for the flux-weakening controller is:

$$\begin{cases} \frac{dX_{vci}}{dt} = v_{\mathrm{cmax}}^* - v_c \\ i_{dref} = k_{vci}X_{vci} + k_{vcp}(v_{\mathrm{cmax}}^* - v_c) \end{cases} \tag{2}$$

where k_{vci} and k_{vcp} are the integral gain and proportional gain for the flux-weakening controller, X_{vci} is the state variable introduced by the integral component of the PI controller, $v_{\mathrm{cmax}}^* = v_{dc}/\sqrt{3}$, and $v_c = \sqrt{v_d^2 + v_q^2}$.

The differential equation for the droop controller is:

$$\begin{cases} \frac{dX_{dci}}{dt} = v_{dc}^* - v_{dc} \\ i_{qref} = k_{dci}X_{dci} + k_{dcp}\left(v_{dc}^* - v_{dc}\right) \end{cases} \tag{3}$$

where k_{dci} and k_{dcp} are the integral gain and proportional gain for droop controller, X_{dci} is the state variable introduced by the droop controller, and v_{dc} is the DC bus voltage. The voltage reference value v_{dc}^* varies depending on the power allocation mode:

$$v_{dc}^* = \left(P_{ref} - P\right)k_{droop} + V_{base} \tag{4}$$

where P_{ref} represents the reference output power of the PMSG obtained through the power allocation strategy, $P = i_{dc}v_{dc}$ is the actual output power of the PMSG, k_{droop} is the droop coefficient, and V_{base} is the rated DC bus voltage.

The input of the current inner loop is the error between the detected actual current value and the current reference value from the outer loop. The output is the control voltage. The differential equation set for the current controller is:

$$\begin{cases} \frac{dX_{idi}}{dt} = i_{dref} - i_d \\ \frac{dX_{iqi}}{dt} = i_{qref} - i_q \\ z_d = k_{idi}X_{idi} + k_{idp}\left(i_{dref} - i_d\right) \\ z_q = k_{iqi}X_{iqi} + k_{iqp}\left(i_{qref} - i_q\right) \end{cases} \tag{5}$$

where k_{idi}, k_{iqi}, k_{idp} and k_{iqp} are the integral gain and proportional gain for current controller. X_{idi} and X_{iqi} are the state variables associated with the PI controllers.

Typically, a rectifier consists of a bridge circuit comprising six IGBTs, which control IGBT switching according to the control objective to generate PWM signals [29]. The rectifier is modeled using an average value model:

$$\begin{cases} u_d = d_d v_{dc} \\ i_{dc} = \frac{3}{2}\left(d_d i_d + d_q i_q\right) \\ u_q = d_q v_{dc} \end{cases} \tag{6}$$

where i_{dc} is the output current of the PMSG and d_d and d_q are the modulation indexes.

Following the rectifier, a DC bus capacitor is described by the following differential equation:

$$\frac{dv_{dc}}{dt} = \frac{i_{dc} - i_o}{C_{dc}} \tag{7}$$

where C_{dc} is the DC-link capacitor and i_o is the output current of the PMSG.

2.2. Supercapacitor and Bidirectional DC-DC Converter Model

The supercapacitor employs a bidirectional boost–buck converter as the interface between the energy storage device and the DC bus [30]. The control diagram of the supercapacitor is shown in Figure 4.

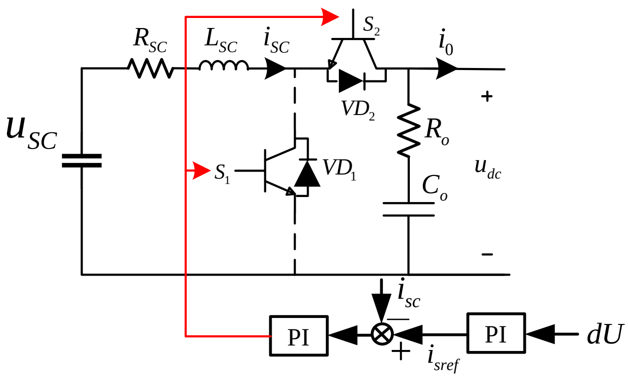

Figure 4. Control diagram of supercapacitor.

The differential equation set for the supercapacitor and its bidirectional DC-DC converter can be represented as follows:

$$\begin{cases} \frac{di_{SC}}{dt} = \frac{v_{SC} - (1-d)v_{osc} - R_{SC} \cdot i_{SC}}{L_{SC}} \\ \frac{dv_{co}}{dt} = \frac{(1-d)i_{SC} - i_{osc}}{C_o} \\ \frac{dv_{SC}}{dt} = \frac{i_{SC}}{C_{SC}} \\ i_{osc} = \frac{v_{co} + (1-d)R_o i_{SC} - v_{osc}}{R_o} \end{cases} \tag{8}$$

where the duty cycle d is generated by the controller of the DC-DC converter and changes with variations in the system's state or output variables.

The expression for the voltage loop PI controller is:

$$\begin{cases} \frac{dX_i}{dt} = K_{isi} dU \\ i_{sref} = K_{isp} dU + X_i \end{cases} \tag{9}$$

where dU is the voltage difference, obtained from the following equation:

$$dU = \left(v_{dc}^* - v_{osc} - \frac{1}{2}P_{diff}\right) \times 1.2 \times \left(1 - \frac{i_{sc} v_{sc}}{P_{sc}^{rated}}\right) \times 0.7 \times 1.2 \tag{10}$$

The expression for the current loop PI controller is:

$$\begin{cases} \frac{dX_d}{dt} = K_{ddi}\left(i_{sref} - i_{sc}\right) \\ d = K_{ddp}\left(i_{sref} - i_{sc}\right) + X_d \end{cases} \tag{11}$$

where k_{isp}, k_{isi}, k_{ddp} and k_{ddi} are the proportional and integral parameters in the voltage and current controllers.

2.3. Voltage Setting under Different Power Allocation Modes

Based on different power allocation modes, the voltage setpoint of the voltage outer loop controller for diesel generator 1, which is obtained from the droop control, is:

(1) Specified power operation

Representing the specified output power of diesel generator 1 by R, the voltage setpoint for generator 1 is:

$$v_{dc1}^* = \begin{cases} (P_{whole}/2 - P_1)k_{droop}/1000 + V_{base}, \text{ when } R > P_{whole} \\ (R - P_1)k_{droop}/1000 + V_{base}, \text{ when } R < P_{whole} \end{cases} \tag{12}$$

where P_1 is the output power of generator 1 and P_{whole} is the load power.

(2) Specified proportional operation

Representing the specified output power of diesel generator 1 as a proportion of the total power by Q, the voltage setpoint for generator 1 is:

$$v_{dc1}^* = \begin{cases} (QP_{whole} - P_1)k_{droop}/1000 + V_{base}, \text{ when } QP_{whole} < 500 \\ (500,000 - P_1)k_{droop}/1000 + V_{base}, \text{ when } QP_{whole} > 500 \end{cases} \tag{13}$$

(3) Full load operation of generator 1

When the total load power exceeds 500 kW, generator 1 takes on 500 kW, and the remaining power is borne by generator 2. When the total power is less than 500 kW, both generators share the total power equally. Thus, the voltage setpoint for generator 1 is:

$$v_{dc1}^* = \begin{cases} (P_{whole}/2 - P_1)k_{droop}/1000 + V_{base}, \text{ when } P_{whole} < 500 \\ (500,000 - P_1)k_{droop}/1000 + V_{base}, \text{ when } P_{whole} > 500 \end{cases} \tag{14}$$

(4) Full load operation of generator 2

When the total load power exceeds 500 kW, generator 2 takes on 500 kW, and the remaining power is borne by generator 1. When the total power is less than 500 kW, both generators share the total power equally. Thus, the voltage setpoint for generator 1 is:

$$v_{dc1}^* = \begin{cases} (P_{whole}/2 - P_1)k_{droop}/1000 + V_{base}, \text{ when } P_{whole} < 500 \\ (P_{whole} - 500,000 - P_1)k_{droop}/1000 + V_{base}, \text{ when } P_{whole} > 500 \end{cases} \tag{15}$$

(5) Even power distribution

When the power management module is not involved in regulation, the output power of the two diesel generators is evenly distributed. Thus, the voltage setpoint for generator 1 is:

$$v_{dc1}^* = (P_{whole}/2 - P_1)k_{droop}/1000 + V_{base} \tag{16}$$

Regardless of the power allocation method, if the difference between the total power and the power of generator 1 exceeds 500 kW, generator 2 can bear a maximum of 500 kW.

If the difference is less than 500 kW, the DC reference voltage of generator 2 is set to 710 V. Thus, the voltage setpoints for generator 2 are both:

$$v_{dc2}^{*} = \begin{cases} V_{base}, \text{when } P_{whole} - P_1 < 500 \text{ kW} \\ (500,000 - P_2)k_{droop}/1000 + V_{base}, \text{ when } P_{whole} - P_1 > 500 \text{ kW} \end{cases} \tag{17}$$

2.4. Small-Signal Model of DC Distribution SPS

The system loads are modeled using a constant power load (CPL), since the most significant load in SPS is often the propulsion load, which exhibits characteristics of a CPL. Applying Kirchhoff's current and voltage laws, we can calculate:

$$i_{o1} + i_{o2} + i_{SC} = i_{load} = \frac{P_{load}}{v_{dc}} \tag{18}$$

where P_{load} is the power of the CPL.

Hence, the model for the entire system can be obtained as:

$$\dot{x} = f(x, u) \tag{19}$$

where x represents the system state variables:

$$\begin{aligned} x = \ & [i_{d1}, i_{q1}, V_{dc1}, X_{vci1}, X_{ioi1}, X_{idi1}, X_{iqi1}, V_{d1}, V_{q1}, \\ & i_{d2}, i_{q2}, X_{vci2}, X_{ioi2}, X_{idi2}, X_{iqi2}, V_{d2}, V_{q2}, i_{sc}, V_{sc}, V_{co}, X_i, X_d] \end{aligned} \tag{20}$$

The input of the system is $u = [i_o]$.

Linearizing at the equilibrium point yields the small-signal model of the entire DC distribution SPS:

$$\delta\dot{x} = A(x_0, u_0)\delta x + B(x_0, u_0)\delta u \tag{21}$$

and $$\begin{aligned} \delta x = \ & [\delta i_{d1}, \delta i_{q1}, \delta V_{dc1}, \delta X_{vci1}, \delta X_{ioi1}, \delta X_{idi1}, \delta X_{iqi1}, \delta V_{d1}, \delta V_{q1}, \\ & \delta i_{d2}, \delta i_{q2}, \delta X_{vci2}, \delta X_{ioi2}, \delta X_{idi2}, \delta X_{iqi2}, \delta V_{d2}, \delta V_{q2}, \delta i_{sc}, \delta V_{sc}, \delta V_{co}, \delta X_i, \delta X_d] \end{aligned},$$
$\delta u = [\delta i_o]$.

where $A(x_0, u_0)$ is the Jacobian matrix.

3. Small-Signal Stability Analysis of the DC SPS

In this section, the impact of integrating supercapacitors into DC SPS under the parallel operation of two PMSGs is investigated. All system parameters are listed in Table 1. Through quantitative numerical simulations and qualitative analyses, the key influencing factors of system stability under different operating conditions with supercapacitor integration are analyzed.

Table 1. Parameters of DC SPS.

Parameter	Value	Parameter	Value	Parameter	Value
Stator resistance R	0.00168 Ω	Droop controller k_{dcp}	4	SC resistance R_{SC}	0.01 Ω
Stator inductance L_d	296.71 μH	Droop controller k_{dci}	0.04	SC inductance L_{SC}	0.48 mH
Stator inductance L_q	671.74 μH	Flux-weakening controller k_{vcp}	0.1	SC capacitance C_{SC}	1315 F
Permanent magnets flux ψ_f	0.5882 Wb	Flux-weakening controller k_{vci}	0.4	Converter resistance R_o	1 mΩ
Rotor speed ω_e	1500 r/min	dq-axes current controller k_{idp}, k_{iqp}	0.6	Converter capacitance C_o	470 μF
Rated DC bus voltage V_{base}	710 V	dq-axes current controller k_{idi}, k_{iqi}	0.005	SC voltage controller k_{isp}	40
DC-link capacitor C_{dc}	9.6 mF	Droop coefficient k_{droop}	0.5	SC voltage controller k_{isi}	1.2
Load power P_{load}	900 kW	SC current controller k_{ddp}	0.0001	SC current controller k_{ddi}	0.01

3.1. Eigenvalue and Influence Factor Analysis

Under the scenario of the parallel operation of diesel generator sets and integration of supercapacitors into the DC distribution system with a load resistance of 0.56 Ω, five power allocation methods are employed. Stability points and Jacobian matrices are computed, and the eigenvalues of the system and the corresponding influence factors of each state variable are determined. The system's eigenvalues are depicted in Figure 5.

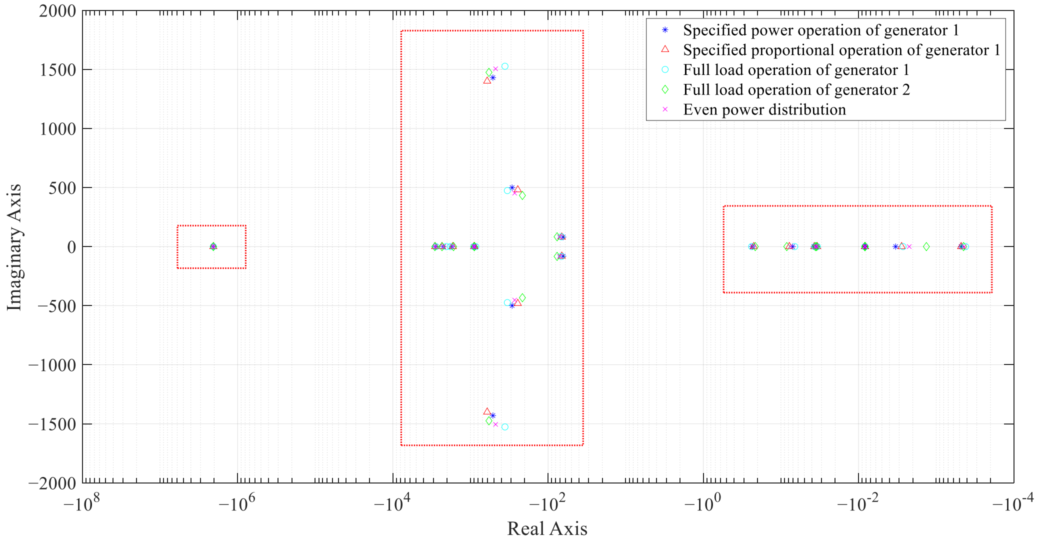

Figure 5. Eigenvalue distribution diagram for DC SPS.

As illustrated in Figure 5, the eigenvalue distribution clearly demonstrates that, irrespective of the power allocation method employed, all eigenvalues are positioned within the left half-plane. This placement unequivocally indicates that the system is in a stable state. Furthermore, to provide a more detailed analysis, three distinct regions have been identified within the eigenvalue distribution, as highlighted by the red boxes in the figure. These regions are categorized based on stability margins, specifically: high stability margin region, medium stability margin region, and low stability margin region. This emphasizes that while the high and medium stability margin regions, due to their considerable distance from the imaginary axis, generally do not affect the system's stability, the low stability margin region warrants closer scrutiny.

Taking the case of generator 1 operating under specified power as an example, specific eigenvalues along with their corresponding damping ratios and oscillation frequencies are provided in Table 2.

Table 2. Eigenvalues at equilibrium point.

Modes	Eigenvalues	Oscillation Frequency (Hz)	Damping Ratio
λ_1	−2,052,086.86731952	0	1
λ_2	−2813.87796089011	0	1
$\lambda_{3,4}$	−513.685428 ± 1430.090132i	227.61	0.3381
λ_5	−2242.95751724705	0	1
λ_6	−1727.77908001236	0	1
$\lambda_{7,8}$	−290.581350 ± 499.169328i	79.45	0.5031
λ_9	−908.052768727717	0	1
λ_{10}	−878.117038296823	0	1
$\lambda_{11,12}$	−63.991103 ± 80.805590i	12.86	0.6208
λ_{13}	−0.233753676376449	0	1
λ_{14}	−0.0707079747222522	0	1
λ_{15}	−0.0375952333943950	0	1
λ_{16}	−0.0342109774845244	0	1
λ_{17}	−0.000477508996369423	0	1
λ_{18}	−0.00333148924301486	0	1
λ_{19}	−0.00827033338498268	0	1
λ_{20}	−0.00827266388874288	0	1
λ_{21}	−0.00826478841142583	0	1
λ_{22}	−0.00825987344527088	0	1

In Table 2, most of the eigenvalues have an imaginary part of zero and a damping ratio of 1, indicating an overdamped state where small disturbances do not induce oscillations in the system. Among the 22 eigenvalues, 16 are negative real roots, corresponding to decaying modes. $\lambda_{3,4}$, $\lambda_{7,8}$, and $\lambda_{11,12}$ are negative eigenvalues corresponding to three oscillatory modes with oscillation frequencies of 234.26 Hz, 79.45 Hz, and 12.86 Hz, respectively. The damping ratio of $\lambda_{3,4}$ is not high, suggesting that insufficient damping may be provided to suppress low-frequency oscillations when the system experiences small disturbances. Conversely, $\lambda_{11,12}$ has a slightly lower oscillation frequency but a relatively higher damping ratio.

The influence factors are computed to determine the state variables associated with low-frequency oscillations, as shown in Table 3.

Table 3. Eigenvalues and corresponding state variable influence factors.

Modes	Impact Factors
λ_1	V_{dc1}2.5%, V_{co}97.5%
λ_2	i_{d1}74.6%, i_{q1}8.2%, V_{d1}15.1%, V_{q1}1.2%
$\lambda_{3,4}$	i_{d1}7%, i_{q1}44.5%, V_{dc1}2.8%, V_{d1}6.1%, V_{q1}38.6%
λ_5	V_{dc1}5.1%, i_{d2}43.4%, i_{q2}3.1%, V_{d2}28%, V_{q2}19.6%
λ_6	V_{dc1}13.2%, i_{d2}8.3%, i_{q2}12.4%, V_{d2}20.1%, V_{q2}44.7%
$\lambda_{7,8}$	i_{q1}3.1%, V_{dc1}39.5%, i_{d2}1.9%, i_{q2}34.7%, V_{d2}3.2%, V_{q2}8.8%, i_{sc}5.3%
λ_9	i_{d1}11.2%, V_{d1}70.8%, V_{q1}17.8%
λ_{10}	i_{d2}13.6%, i_{q2}2.6%, V_{d2}70.5%, V_{q2}13.2%
$\lambda_{11,12}$	V_{dc1}5.2%, i_{q2}3.9%, i_{sc}45%, X_d44.6%
λ_{13}	X_{vci1}1.6%, X_{dci1}95.4%, X_{dci2}2.4%
λ_{14}	X_{vci1}1.6%, X_{dci1}3%, X_{vci2}19.1%, X_{dci2}58.5%, X_i17.6%
λ_{15}	X_{vci1}14.7%, X_{dci1}1.9%, X_{vci2}64.7%, X_{dci2}8.7%, X_i9.9%
λ_{16}	X_{vci1}75%, X_{vci2}22.2%, X_i2.2%
λ_{17}	V_{sc}49.9%, X_i49.4%
λ_{18}	X_{dci2}6%, V_{sc}49.9%, X_i44%
λ_{19}	X_{idi1}39.2%, X_{iqi1}10.7%, X_{idi2}38.5%, X_{iqi2}11.4%
λ_{20}	X_{idi1}49.5%, X_{idi2}48.9%
λ_{21}	X_{iqi1}49.7%, X_{iqi2}49.3%
λ_{22}	X_{idi1}19.2%, X_{iqi1}30.7%, X_{idi2}11.1%, X_{iqi2}38.9%

Through the analysis of influence factors, the impact of system state variables on eigenvalues is discernible. Specifically, λ_1 is primarily associated with V_{co}, which relates to the DC/DC converter output capacitor voltage. Given its significant distance from the imaginary axis, λ_1's impact on system stability is minimal. λ_2, predominantly influenced by the d-axis stator current and voltage of generator 1 and also situated far from the imaginary axis, exerts little effect on system stability. λ_3 and λ_4, chiefly affected by the q-axis stator current and voltage of generator 1, are influenced by the droop control coefficient. λ_5 and λ_6, related to the stator current and voltage of generator 2 and DC bus state variables, respectively, are located far from the imaginary axis and hence have a minimal influence on stability. λ_7 and λ_8, associated with the q-axis stator current of both generators and DC bus state variables, are influenced by DC bus voltage and the PMSG voltage controller. λ_9 and λ_{10}, related to the stator voltage of generator 1 and 2, respectively, are also distant from the imaginary axis. λ_{11} and λ_{12}, related to the supercapacitor output current and its current loop controller, represent a pair of dominant conjugate roots introduced by supercapacitor integration. λ_{17} and λ_{18} are associated with the supercapacitor voltage and its outer voltage controller. λ_{13} to λ_{16} and λ_{19} to λ_{22}, related to the outer voltage controllers, flux-weakening controllers, and d-axis and q-axis current control inner loops of both generator units, are influenced by PI controller parameters. However, compared to the electromagnetic transient time constants of the generators and rectifiers, their inertia time constants are considerably larger, resulting in very small variations in eigenvalues and thus a lesser impact on system stability.

From the preceding analysis, it is concluded that the integration of supercapacitors into the DC distribution system primarily affects the trajectories of five key eigenvalues: λ_1, λ_{11}, λ_{12}, λ_{17}, and λ_{18}. Notably, λ_{11} and λ_{12} are conjugate roots; serving as the dominant modes with relatively lower oscillation frequencies, they are particularly sensitive to variations in supercapacitor parameters. The specific effects of these electrical and control parameters on the stability are analyzed theoretically under different conditions.

3.2. Impact of Capacitance and Resistance Parameter Variations on Converter Output

At the interface between the DC/DC converter and the DC bus, a pair of series-connected capacitor C_o and resistor R_o are paralleled. Here, the influence of parameter variations on the system stability is analyzed. Employing the same power allocation method for generator 1 operating at specified power, trajectories of λ_{11} and λ_{12} are calculated as C_o gradually increases from 0.1 mF to 100 mF, as depicted in Figure 6.

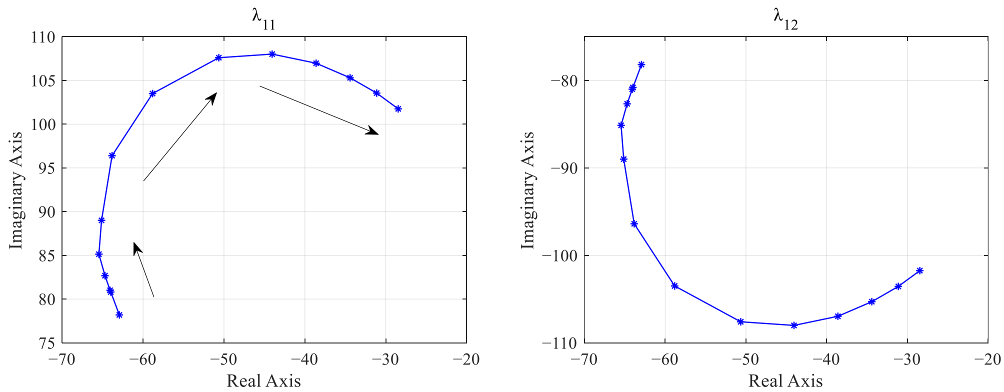

Figure 6. Eigenvalue trajectories with varying C_o values.

In Figure 6, the blue asterisk represents the location of eigenvalues in the s-plane. The arrows, on the other hand, indicate the direction of movement for these eigenvalues as the C_o increase. It can be observed that as the output capacitance of the converter increases, the eigenvalues gradually approach the imaginary axis in an arc shape, but always remain on the left-hand side of the imaginary axis, indicating stability within this range.

Similarly, with R_o gradually increasing from 1 mΩ to 1 Ω, the trajectories of λ_{11} and λ_{12} with R_o are calculated, as shown in Figure 7.

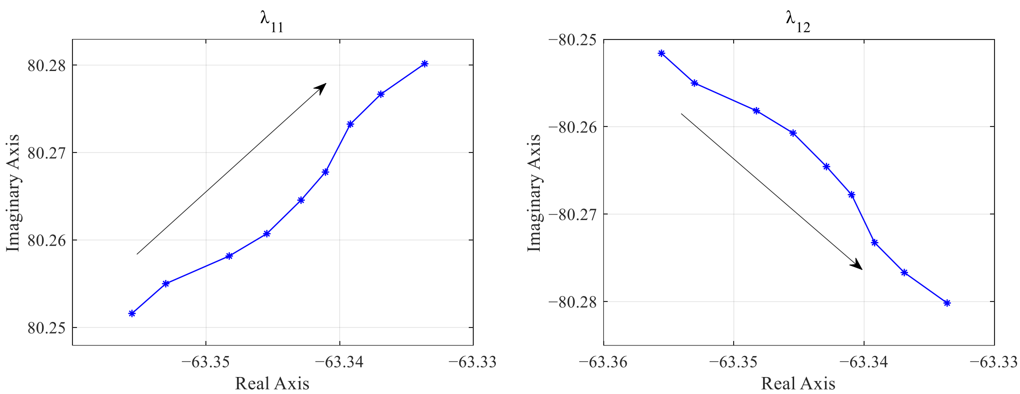

Figure 7. Eigenvalue trajectories with varying R_o values.

From Figure 7, it can be observed that as the output resistance of the converter increases, the eigenvalues move very slowly towards the imaginary axis, indicating that the variation of R_o has minimal impact on the eigenvalues and virtually no effect on the stability of the system.

3.3. Impact of Inductance and Resistance Parameter Variations on Converter Input

The input stage of the supercapacitor and DC/DC converter is connected in a series with a pair of inductors L_{sc} and resistors R_{sc}. Here, the influence of parameter variations on the system stability is analyzed. When L_{sc} gradually increases from 0.1 mH to 10 mH, the trajectories of λ_{11} and λ_{12} are computed with respect to the variation, as shown in Figure 8.

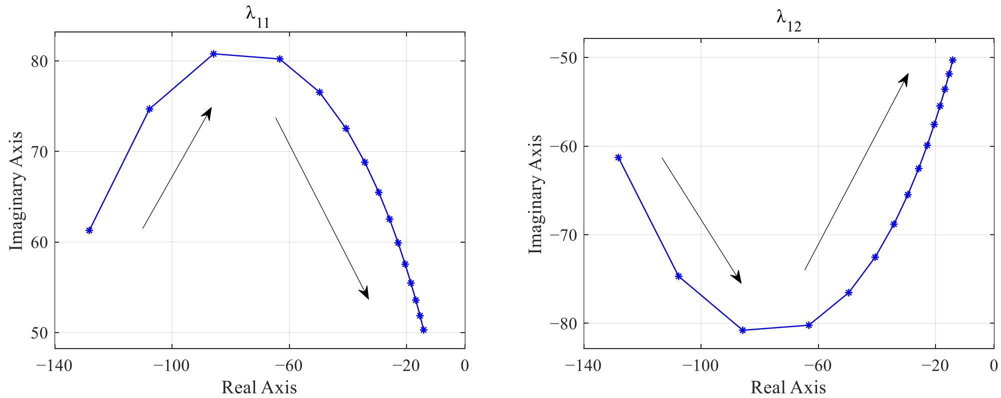

Figure 8. Eigenvalue trajectories with varying L_{sc} values.

As shown in Figure 8, as L_{sc} gradually increases, the dominant low-frequency eigenvalues approach the imaginary axis but do not cross it. This indicates that the variation in the input inductance of the converter has a minor impact on the system stability. However, it is worth noting that when the value of L_{sc} becomes excessively large, the dominant low-frequency eigenvalues may shift to the right half-plane, causing the system to lose stability.

When R_{sc} increases gradually from 1 mΩ to 50 Ω, the trajectories of λ_{11} and λ_{12} with respect to the variation are computed, as shown in Figure 9.

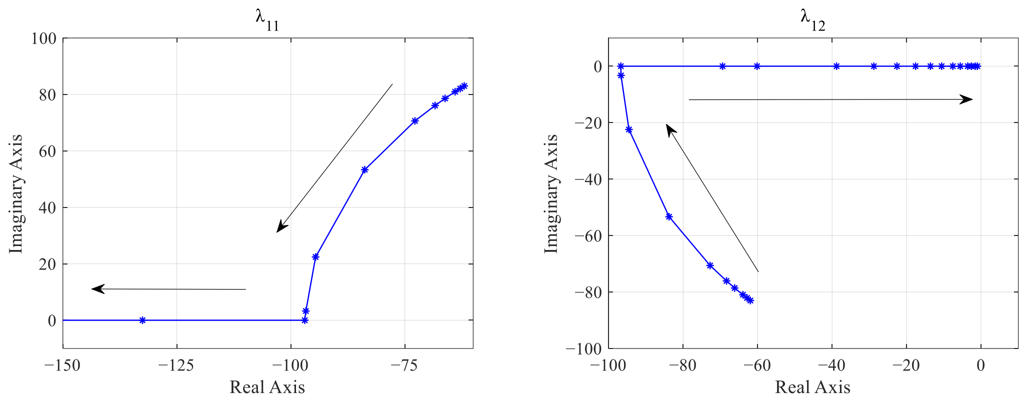

Figure 9. Eigenvalue trajectories with varying R_{sc} values.

As shown in Figure 9, when R_{sc} exceeds 5 mΩ, two eigenvalues converge on the real axis and move in opposite directions along the real axis. With the increase in the input resistance of the converter, the rate at which λ_{12} approaches the imaginary axis slows down, while the speed at which λ_{11} moves away from the imaginary axis increases. Even when R_{sc} reaches 50, λ_{12} continues its gradual approach towards the imaginary axis without crossing into the right half-plane, thus maintaining stability. Therefore, the system remains stable within the range where R_{sc} is less than 50 Ω.

3.4. Impact of Supercapacitor Voltage Controller PI Parameter Variation

The voltage controller input is composed of the voltage difference multiplied by the output power control coefficient, and the output of the PI controller regulates the reference value of the super capacitor output current. To analyze the impact of the voltage control loop on the system stability, increasing k_{isp} and k_{isi} separately, the root locus of the characteristic values λ_{11} and λ_{12} with k_{isp} variation is obtained, as shown in Figure 10.

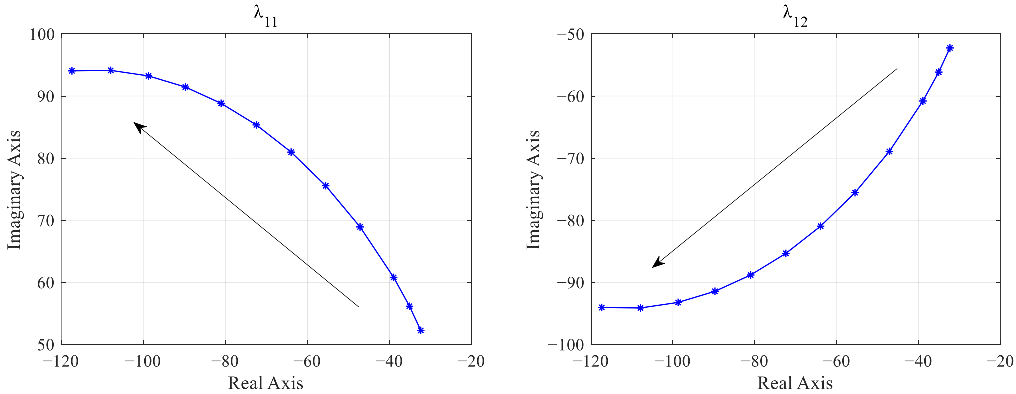

Figure 10. Eigenvalue trajectories with varying k_{isp} values.

From Figure 10, it can be observed that as k_{isp} increases gradually from 1 to 100, the real parts of the dominant characteristic roots affecting system stability will also gradually shift leftwards towards the real axis, indicating an improvement in system stability.

The root locus of the characteristic roots for the voltage outer loop, as shown in Figure 11, indicates that as k_{isi} increases from 0.1 to 10, the roots λ_{11} and λ_{12} gradually approach the imaginary axis, but they never cross it, indicating system stability within this range.

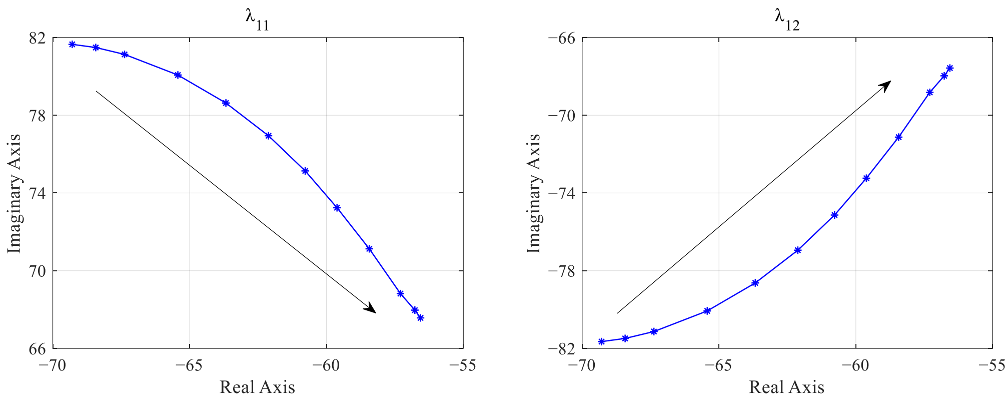

Figure 11. Eigenvalue trajectories with varying k_{isi} values.

3.5. Impact of Supercapacitor Current Controller PI Parameter Variation

The current controller is responsible for generating the modulation signal for the DC/DC converter. It calculates the difference between the reference current value for the supercapacitor output and the actual current value to obtain the current error. Subsequently, the PI controller adjusts this error to generate the modulation signal. This modulation signal, after PWM modulation, eventually controls the switching devices by controlling on and off states. To analyze the effect of the voltage control loop on system stability, the PI parameters of the current inner loop, namely k_{ddp} and k_{ddi}, are individually increased. The resulting characteristic roots and their trajectories with parameter variations are depicted in Figure 12.

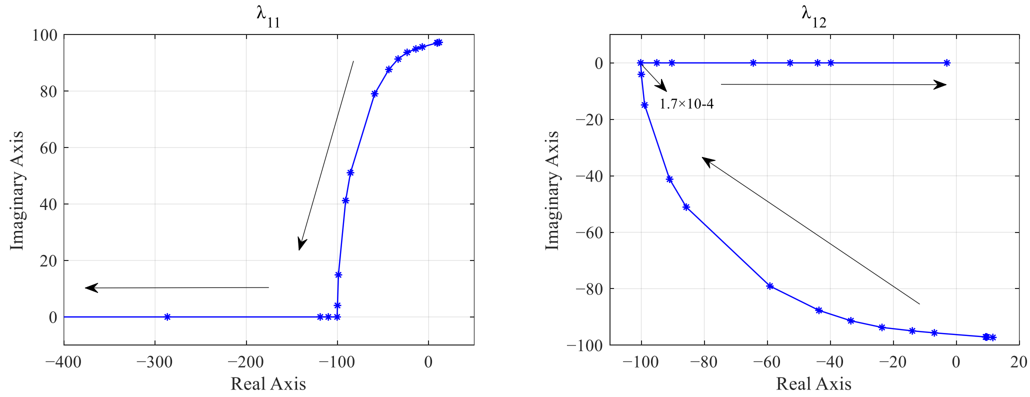

Figure 12. Eigenvalue trajectories with varying k_{ddp} values.

As depicted in Figure 12, when k_{ddp} increases from 1×10^{-6} to 1, λ_{11} and λ_{12} move from the right half-plane to the left half-plane of the s-domain with the increase in k_{ddp}, crossing the imaginary axis into the left half-plane when k_{ddp} exceeds 9×10^{-6}, indicating the system's transition to stability. At $k_{ddp} = 1.7 \times 10^{-4}$, the two eigenvalues intersect with the real axis and then move in opposite directions along it. As k_{ddp} continues to increase, λ_{12} approaches the imaginary axis very slowly and does not cross it even at $k_{ddp} = 1$. Due to the inherent upper and lower limits of the PI controller, further increases in k_{ddp} are inconsequential. Hence, the system remains stable within the range where k_{ddp} is greater than 9×10^{-6}.

Figure 13 depicts the root locus of the characteristic roots as k_{ddi} increases from 0.001 to 1. It can be observed that λ_{11} and λ_{12} gradually approach the imaginary axis with increasing k_{ddi}. When k_{ddi} reaches 0.15, the characteristic values cross the imaginary axis into the right half-plane of the s domain, causing system instability. This indicates that under the specified operating conditions, the system remains stable when k_{ddi} is less than 0.15; however, when k_{ddi} exceeds 0.15, the system enters the right side of the imaginary axis, becoming unstable.

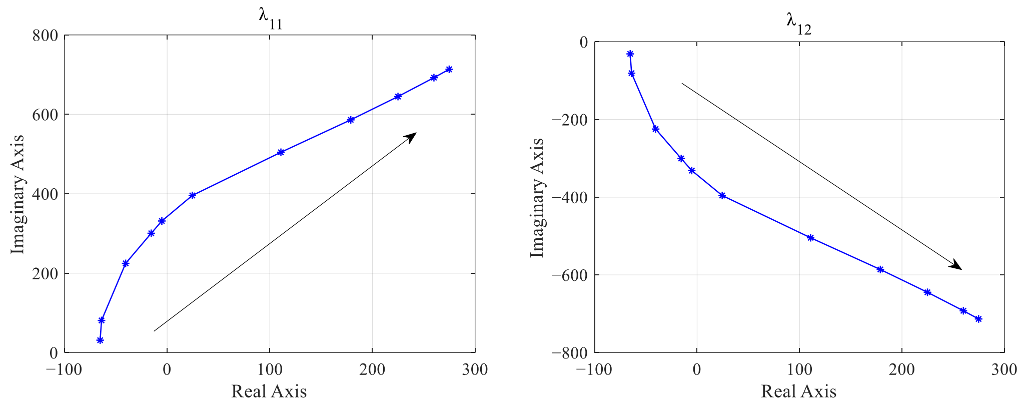

Figure 13. Eigenvalue trajectories with varying k_{ddi} values.

4. Simulation Verification

In this section, the small-signal stability of SPS integrated with a supercapacitor is examined through case studies. The impact of newly introduced electrical and control parameters on system stability after the integration of a supercapacitor are explored through simulation experiments, as illustrated in Figure 14. The selection and adjustment of PI parameters for controlling the charging and discharging of the supercapacitor not only affect the performance of the supercapacitor but also directly influence the overall system stability.

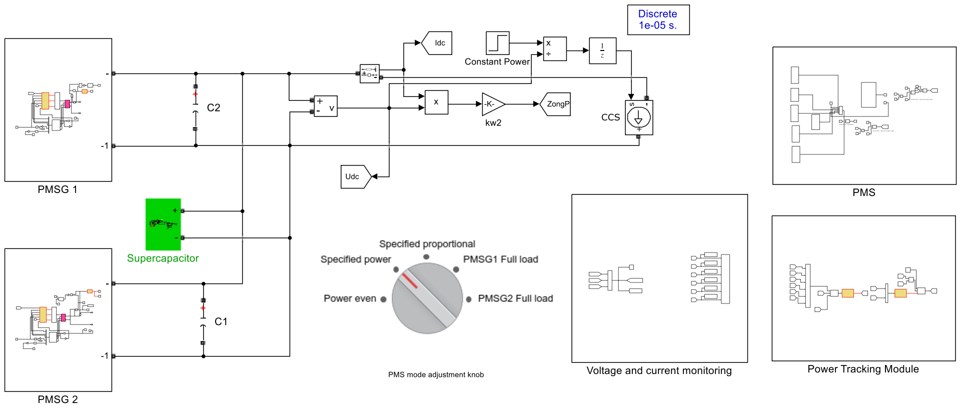

Figure 14. Simulation model for DC SPS in MATLAB R2022a.

4.1. Case 1

In this case, a comprehensive simulation analysis was conducted to investigate the impact of varying proportional gain k_{ddp} of the current controller on system stability. Specifically, k_{ddp} was set at values of 1×10^{-6}, 5×10^{-6}, 1×10^{-5}, and 1×10^{-4}, aiming to explore how changes in this parameter affect the dynamic behavior and stability of the system. Simulation curves are shown in Figures 15 and 16.

The simulation results revealed several key observations. At lower k_{ddp} values of 1×10^{-6}, significant oscillations in the DC bus voltage and current were observed, indicating system instability. As k_{ddp} was increased to 5×10^{-6}, although oscillations persisted in the voltage curve, the amplitude of these oscillations decreased, suggesting an improvement in system stability, albeit not yet reaching an ideal state of stability. These oscillations not only signify an unstable system state but also suggest that the lower k_{ddp} values do not provide sufficient control strength to counteract disturbances. The presence of these oscillations directly impacts system reliability and performance, exposing the system's vulnerability under these parameter settings.

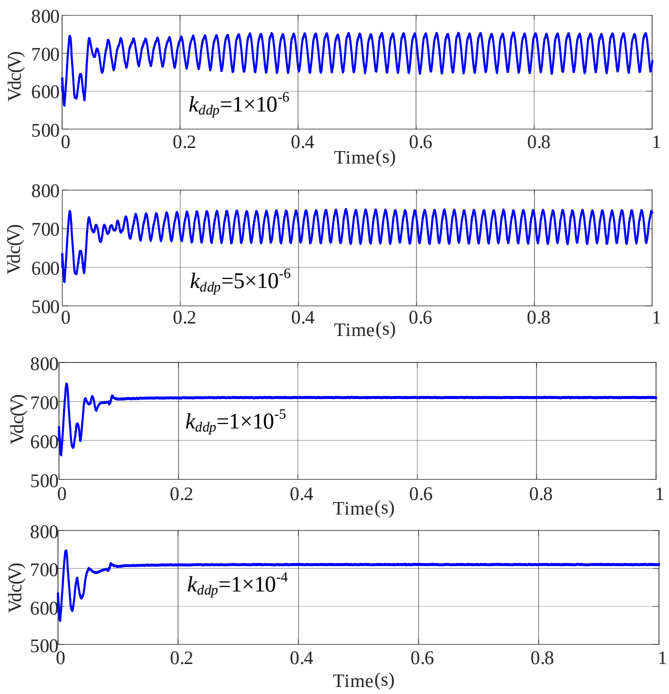

Figure 15. DC bus voltage curves for different k_{ddp} values.

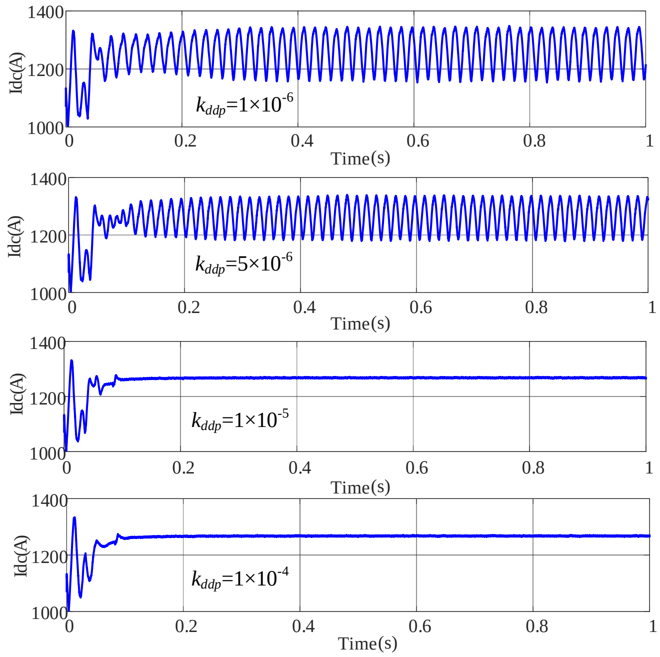

Figure 16. DC bus current curves for different k_{ddp} values.

With an increase in k_{ddp} to 1×10^{-5} and 1×10^{-4}, a marked improvement in system performance was noted. Particularly, when k_{ddp} reached 1×10^{-5}, the amplitude of oscillations in the DC bus voltage and current significantly reduced, indicating the onset of system stability. At k_{ddp}=1×10^{-4}, the system exhibited stable responses in both DC bus voltage and current without noticeable oscillations, demonstrating that higher k_{ddp} values effectively enhance the system's ability to resist disturbances and bolster stability.

These simulation outcomes unequivocally demonstrate the decisive role of the current controller's proportional gain k_{ddp} in the stability of DC SPS. Lower k_{ddp} values lead to diminished system stability, whereas an increase in k_{ddp} significantly enhances stability.

4.2. Case 2

In case 2, the integral gain k_{ddi} was methodically adjusted to values of 0.01, 0.1, 0.15, and 0.2 in distinct simulation experiments. This setup aimed to scrutinize the influence of k_{ddi} adjustments on the system's dynamic stability and operational behavior. The simulation curves are illustrated in Figures 17 and 18.

The simulation findings presented a detailed narrative of how k_{ddi} influences system stability. For k_{ddi} values set at 0.01 and 0.1, the system exhibited stable responses with the DC bus voltage and current maintaining equilibrium without significant fluctuations. This stability indicates that at these levels, k_{ddi} provides adequate damping to system perturbations, ensuring robust system performance under varying operational conditions.

However, as k_{ddi} increased to 0.15 and further to 0.2, the stability of the system was compromised. Specifically, simulations at these higher k_{ddi} settings revealed pronounced oscillations in both the DC bus voltage and current, signifying a transition to an unstable system state. The emergence of these oscillations at higher k_{ddi} values indicates an overcompensation in the system's response to disturbances, leading to instability. The oscillation amplitude approached nearly ±10%, a deviation that significantly breaches the system performance criteria.

These insights from the simulation analysis align with the theoretical results in Section 3.5 and confirm the critical role of the current controller's integral gain k_{ddi} in maintaining system stability. While lower k_{ddi} values ensure system stability by effectively damping oscillations, exceeding a threshold (k_{ddi} > 0.15) precipitates instability.

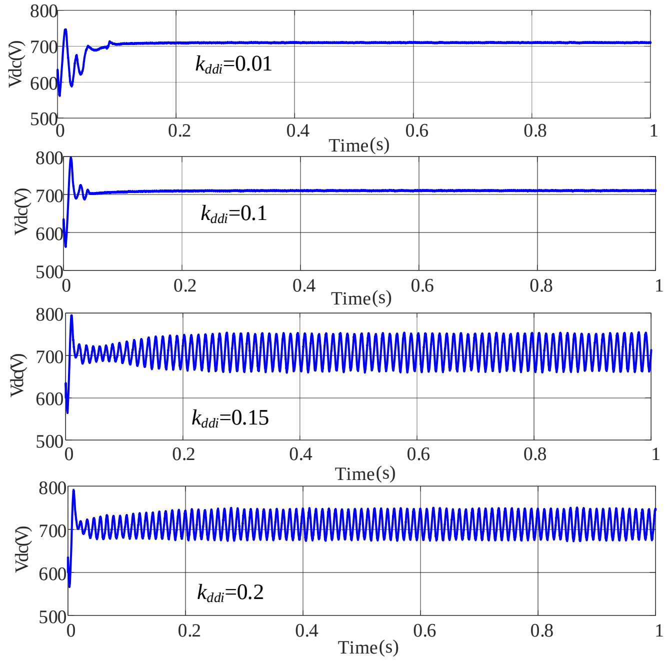

Figure 17. DC bus voltage curves for different k_{ddi} values.

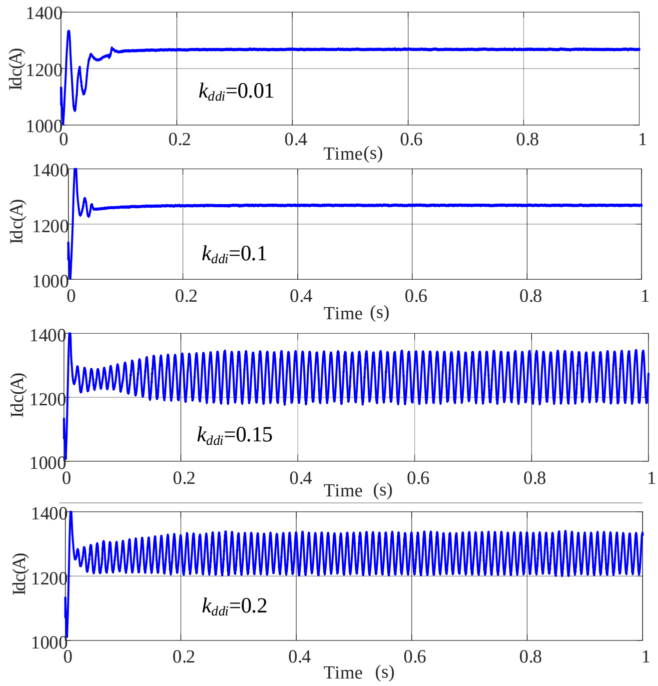

Figure 18. DC bus current curves for different k_{ddi} values.

5. Conclusions

This study investigated the small-signal stability of integrating supercapacitors into a DC SPS. The control model for PMSG and their small-signal models were formulated, featuring a detailed analysis of PMSG parallel operations across five power distribution modes. The specific impacts of newly introduced electrical and control parameters, including the input-output parameters of converters and the PI controllers' parameters of supercapacitor controllers, on system stability were explored following the integration of supercapacitors. Simulations conducted using MATLAB revealed that the converter's input-output electrical parameters have a negligible influence on eigenvalues and overall system stability. It was found that system stability increases with k_{ddp} and stabilizes when

k_{ddp} exceeds 5×10^{-6}, maintaining stability when k_{ddi} is below 0.15, but instability occurs beyond 0.15.

This research highlights that supercapacitor integration can significantly enhance system stability by mitigating oscillations and providing additional damping, especially in dominant modes. The findings illustrate the pivotal role of electrical and control parameter adjustments in leveraging supercapacitor benefits while ensuring the system's resilience. The exploration into the nuanced influences of these parameters under various conditions sheds light on the critical balance between enhancing performance and maintaining system stability.

Future avenues for research may include investigating the effects of modified droop control strategies on power distribution and assessing system behavior under the variable-speed operations of diesel generator sets.

Author Contributions: Conceptualization, Q.Y. and S.W.; Data curation, Q.Y. and X.W.; Formal analysis, W.Z. (Wei Zhuang); Funding acquisition, Q.Y., X.W. and W.Z. (Wanlu Zhu); Investigation, Q.Y.; Methodology, Q.Y. and S.W.; Project administration, X.W.; Resources, W.Z. (Wei Zhuang); Software, W.Z. (Wei Zhuang); Supervision, X.W.; Validation, S.W. and W.Z. (Wei Zhuang); Visualization, S.W.; Writing—original draft, Q.Y. and W.Z. (Wanlu Zhu); Writing—review & editing, W.Z. (Wanlu Zhu). All authors have read and agreed to the published version of the manuscript.

Funding: This research received no external funding.

Institutional Review Board Statement: Not applicable.

Informed Consent Statement: Not applicable.

Data Availability Statement: The data presented in this study are available on request from the corresponding author. The data are not publicly available due to privacy.

Conflicts of Interest: The authors declare no conflicts of interest.

References

1. IEEE Standards Association. *IEEE std. 1709—2018 IEEE Recommended Practice for 1kV to 35 kV Medium-Voltage DC Power Systems on Ships*; IEEE: Piscataway, NJ, USA, 2018.
2. Inal, O.B.; Charpentier, J.F.; Deniz, C. Hybrid power and propulsion systems for ships: Current status and future challenges. *Renew. Sustain. Energy Rev.* **2022**, *156*, 111965. [CrossRef]
3. Coffey, S.; Timmers, V.; Li, R.; Wu, G.; Egea-Àlvarez, A. Review of MVDC applications, technologies, and future prospects. *Energies* **2021**, *14*, 8294. [CrossRef]
4. Xu, L.; Guerrero, J.M.; Lashab, A.; Wei, B.; Bazmohammadi, N.; Vasquez, J.C.; Abusorrah, A. A review of DC shipboard microgrids—Part II: Control architectures, stability analysis, and protection schemes. *IEEE Trans. Power Electron.* **2021**, *37*, 4105–4120. [CrossRef]
5. Liu, S.; Miao, H.; Li, J.; Yang, L. Voltage control and power sharing in DC Microgrids based on voltage-shifting and droop slope-adjusting strategy. *Electr. Power Syst. Res.* **2023**, *214*, 108814. [CrossRef]
6. Latorre, A.; Soeiro, T.B.; Geertsma, R.; Coraddu, A.; Polinder, H. Shipboard DC systems, a Critical Overview: Challenges in Primary Distribution, Power Electronics-based Protection, and Power Scalability. *IEEE Open J. Ind. Electron. Soc.* **2023**, *4*, 259–286. [CrossRef]
7. Hassan, M.A.; Su, C.L.; Pou, J.; Sulligoi, G.; Almakhles, D.; Bosich, D.; Guerrero, J.M. DC shipboard microgrids with constant power loads: A review of advanced nonlinear control strategies and stabilization techniques. *IEEE Trans. Smart Grid.* **2022**, *13*, 3422–3438. [CrossRef]
8. Zeng, Y.; Zhang, Q.; Liu, Y.; Zhuang, X.; Che, L.; Niu, M.; Zheng, X. State-of-charge dynamic balancing strategy for distributed energy storage system in DC shipboard microgrid. *Int. J. Electr. Power Energy Systems* **2021**, *133*, 107094. [CrossRef]
9. Ghimire, P.; Zadeh, M.; Pedersen, E.; Thorstensen, J. Dynamic modeling, simulation, and testing of a marine DC hybrid power system. *IEEE Trans. Transp. Electrif.* **2020**, *7*, 905–919. [CrossRef]
10. Son, Y.K.; Lee, S.Y.; Ko, S.; Kim, Y.W.; Sul, S.K. Maritime DC power system with generation topology consisting of combination of permanent magnet generator and diode rectifier. *IEEE Trans. Transp. Electrif.* **2020**, *6*, 869–880. [CrossRef]
11. Park, D.; Zadeh, M. Dynamic modeling, stability analysis, and power management of shipboard dc hybrid power systems. *IEEE Trans. Transp. Electrif.* **2021**, *8*, 225–238. [CrossRef]
12. Gao, X.P.; Fu, L.J.; Hu, J.; Yan, Q.S. Voltage stability analysis of DC ship power system with pulse load. *J. Eng.* **2019**, *2019*, 2027–2031. [CrossRef]

13. Yang, J.; Yan, H.; Gu, C.; Wang, S.; Zhao, W.; Wheeler, P.; Buticchi, G. Modeling and stability enhancement of a permanent magnet synchronous generator based DC system for more electric aircraft. *IEEE Trans. Ind. Electron.* **2021**, *69*, 2511–2520. [CrossRef]
14. Leng, M.; Zhou, G.; Li, H.; Xu, G.; Blaabjerg, F.; Dragičević, T. Impedance-based stability evaluation for multibus DC microgrid without constraints on subsystems. *IEEE Trans. Power Electron.* **2021**, *37*, 932–943. [CrossRef]
15. Hatziargyriou, N.; Milanovic, J.; Rahmann, C.; Ajjarapu, V.; Canizares, C.; Erlich, I.; Hill, D.; Hiskens, I.; Kamwa, I.; Pal, B.; et al. Definition and classification of power system stability–revisited & extended. *IEEE Trans. Power Syst.* **2020**, *36*, 3271–3281.
16. Ahmed, M.; Meegahapola, L.; Vahidnia, A.; Datta, M. Stability and control aspects of microgrid architectures–a comprehensive review. *IEEE Access* **2020**, *8*, 144730–144766. [CrossRef]
17. Riccobono, A.; Cupelli, M.; Monti, A.; Santi, E.; Roinila, T.; Abdollahi, H.; Arrua, S.; Dougal, R.A. Stability of shipboard dc power distribution: Online impedance-based systems methods. *IEEE Electrif. Mag.* **2017**, *5*, 55–67. [CrossRef]
18. Javaid, U.; Freijedo, F.D.; van der Merwe, W.; Dujic, D. Stability analysis of multi-port MVDC distribution networks for all-electric ships. *IEEE J. Emerg. Sel. Top. Power Electron.* **2020**, *8*, 1164–1177. [CrossRef]
19. Liu, R.; Ding, L.; Xue, C.; Li, Y. Small-signal modelling and analysis of microgrids with synchronous and virtual synchronous generators. *IET Energy Syst. Integr.* **2023**, *4*. [CrossRef]
20. Li, X.; Meng, C.; Yang, Q.; Zhao, Y.; Li, W.; Xie, S.; Jiang, C. Small-signal Stability Analysis of DC Ship Hybrid Power System with Energy Storage Device Based on Hybrid H-matrix Model. *IEEE Trans. Transp. Electrif.* **2023**, 11. [CrossRef]
21. Gao, M.; Liu, J. Parallel Stability Analysis of Generator and Inverter in Independent Micro grid. *J. Phys. Conf. Ser.* **2020**, *1549*, 052004. [CrossRef]
22. Hu, X.; Fan, H.; Li, T.; Meng, Z.; Luo, P.; Zhou, H. Stability analysis and parameter configuration of parallel virtual synchronous generators in microgrid. *Energy Rep.* **2022**, *8*, 866–873. [CrossRef]
23. Xie, P.; Yuan, C.; Guan, Y.; Tan, S.; Li, M.; Vasquez, J.C.; Guerrero, J.M. Stability analysis considering dual physical constraints of parallel-connected virtual synchronous generators forming microgrids. In Proceedings of the 2019 IEEE Energy Conversion Congress and Exposition (ECCE), Baltimore, MD, USA, 29 September 2019–3 October 2019; IEEE: Piscataway, NJ, USA, 2019; pp. 2092–2098.
24. Raza, W.; Ali, F.; Raza, N.; Luo, Y.; Kim, K.H.; Yang, J.; Kumar, S.; Mehmood, A.; Kwon, E.E. Recent advancements in supercapacitor technology. *Nano Energy* **2018**, *52*, 441–473. [CrossRef]
25. Singh, P.; Lather, J.S. Small-signal modeling and stability analysis of autonomous direct current microgrid with distributed energy storage system. *J. Energy Storage* **2021**, *41*, 102973. [CrossRef]
26. Arunkumar, C.R.; Manthati, U.B. Design and small signal modelling of battery-supercapacitor HESS for DC microgrid, TENCON 2019. In Proceedings of the 2019 IEEE Region 10 Conference (TENCON), Kochi, India, 17–20 October 2019; IEEE: Piscataway, NJ, USA, 2019; pp. 2216–2221.
27. Chen, X.; Shi, M.; Sun, H.; Li, Y.; He, H. Distributed cooperative control and stability analysis of multiple DC electric springs in a DC microgrid, IEEE Trans. *Ind. Electron.* **2018**, *65*, 5611–5622. [CrossRef]
28. Sul, S.-K. *Control of Electric Machine Drive Systems*; Wiley: Hoboken, NJ, USA, 2010.
29. Li, Y.; Shuai, Z.; Liu, X.; Hong, Y.; Wu, X.; Shen, Z.J. Stability investigation of bidirectional AC-DC converter considering operating conditions. *IEEE Access* **2020**, *8*, 131499–131510. [CrossRef]
30. Punna, S.; Manthati, U.B.; Raveendran, A.C. Modeling, analysis, and design of novel control scheme for two-input bidirectional DC-DC converter for HESS in DC microgrid applications. *Int. Trans. Electr. Energy Syst.* **2021**, *31*, e12774. [CrossRef]